Additive manufacturing of defect-free TiZrNbTa refractory high-entropy alloy with enhanced elastic isotropy via in-situ alloying of elemental powders

Check for updates

Shahryar Mooraj[1,10], George Kim[2,10], Xuesong Fan[3], Shmuel Samuha[4,5], Yujun Xie[4], Tianyi Li [6],
Jaimie S. Tiley[7], Yan Chen[8], Dunji Yu[8], Ke An [8], Peter Hosemann[4], Peter K. Liaw [3], Wei Chen [2,9] &
Wen Chen [1]

Laser powder-bed fusion (L-PBF) additive manufacturing presents ample opportunities to produce net-shape parts. The complex laser-powder interactions result in high cooling rates that often lead to unique microstructures and excellent mechanical properties. Refractory high-entropy alloys show great potential for high-temperature applications but are notoriously difficult to process by additive processes due to their sensitivity to cracking and defects, such as un-melted powders and keyholes. Here, we present a method based on a normalized model-based processing diagram to achieve a nearly defect-free TiZrNbTa alloy via in-situ alloying of elemental powders during L-PBF. Compared to its as-cast counterpart, the as-printed TiZrNbTa exhibits comparable mechanical properties but with enhanced elastic isotropy. This method has good potential for other refractory alloy systems based on in-situ alloying of elemental powders, thereby creating new opportunities to rapidly expand the collection of processable refractory materials via L-PBF.

Laser powder-bed fusion (L-PBF) is an additive manufacturing (AM) technique that allows for producing near net-shaped parts with a high spatial resolution[1,2]. In L-PBF, a flatbed of powders is spread along a substrate, and a laser is used to melt the powders according to a pre-defined computer-aided design (CAD). This technique employs a highly focused laser with a small beam size to melt feedstock powders to build a part layer by layer[3]. The high energy inputs and rapid scan speeds lead to highly transient laser-powder interactions with high thermal gradients and solidification rates. L-PBF tends to achieve cooling rates on the order of $10^5 - 10^6$ K/s[4–8]. Such high cooling rates can result in highly refined and non-equilibrium microstructures that are not accessible via traditional manufacturing methods, thus opening up a new avenue for materials development[9–11]. In addition, the versatility and freedom offered by the

vast processing space of L-PBF enable tailoring of solidification micro-structures and material properties through different printing conditions[12–17].

High-entropy alloys (HEAs) are a class of alloys that contain multi-principal elements in near-equimolar ratios rather than based on just one or two primary elements in traditional dilute alloys[12,18]. HEAs have been widely studied over the past decade owing to their enormous compositional space for the design of materials with exceptional properties[3,13]. Refractory high-entropy alloys (RHEAs) are a sub-class of HEAs that are composed of multi-principal refractory elements and typically show a body-centered-cubic (BCC) crystal structure. RHEAs hold great promise for high-temperature structural applications due to their ability to maintain high yield strengths at elevated temperatures[18]. For example, Senkov et al. presented a

[1]Department of Mechanical and Industrial Engineering, University of Massachusetts Amherst, Amherst, MA, USA. [2]Department of Mechanical, Materials, and Aerospace Engineering, Illinois Institute of Technology, Chicago, IL, USA. [3]Department of Materials Science and Engineering, University of Tennessee, Knoxville, TN, USA. [4]Department of Nuclear Engineering, University of California, Berkeley, CA, USA. [5]Department of Materials engineering, NRCN, Beer-Sheva, Israel. [6]X-ray Science Division, Argonne National Laboratory, Lemont, IL, USA. [7]Materials Structures and Processing Science Section, Oak Ridge National Laboratory, Oak Ridge, TN, USA. [8]Neutron Scattering Division, Oak Ridge National Laboratory, Oak Ridge, TN, USA. [9]Department of Materials Design and Innovation, University at Buffalo, The State University of New York, Buffalo, NY, USA. [10]These authors contributed equally: Shahryar Mooraj, George Kim.
✉e-mail: wchen226@buffalo.edu; wenchen@umass.edu

AlMo$_{0.5}$NbTa$_{0.5}$TiZr$_{0.5}$ RHEA that can maintain a high yield strength of 935 MPa at temperatures up to 1000 °C[19].

AM of HEAs has recently garnered significant interests due to the exceptional material properties that can be achieved by harnessing the extreme processing conditions (e.g., large thermal gradients, high cooling rates) of AM and the desired compositional effects of HEAs[20–25]. Among HEAs, however, RHEAs are notoriously difficult to process via AM due to the high melting points of the constituent elements and their high sensitivity to cracking[26–29]. The high melting temperatures of refractory elements require high-energy inputs during AM that result in large thermal residual stresses and thus cracking[30,31]. It is difficult to fully melt these high melting-point refractory powders, and the presence of un-melted powders in additively manufactured RHEAs presents a significant challenge[32–36]. For example, additively manufactured VNbMoTaW via L-PBF showed almost no compressive plasticity due to severe cracking[37]. A similar cracking issue limited the performance of a NbMoTa multi-component alloy produced via laser directed energy deposition (L-DED)[38]. In addition to cracking, the excess energy input during AM can also result in evaporation of some constituent elements with lower melting points and thus induce the formation of keyhole pores[39]. Therefore, a delicate balance among the heat input, thermal stresses, and elemental melting/boiling points should be considered to minimize the formation of printing defects in additively manufactured RHEAs.

In the present work, we fabricate nearly defect-free TiZrNbTa RHEAs via L-PBF and in-situ alloying of pure elemental powders. Based on a normalized model-based processing diagram, we identify an effective processing window that accounts for both the energy input and thermophysical properties of the material toward mitigation of processing defects, such as porosity and un-melted powders. Since this processing diagram is built by normalizing the printing parameters against the thermophysical properties of the feedstock materials, the processing method introduced in the current work can be generally extended to other refractory alloy systems. The ability to print defect-free RHEAs via in-situ alloying of elemental powders without the need for expensive pre-alloyed powders opens up ample opportunities for practical development of advanced refractory alloys by AM for high-temperature applications. By systematic analysis of the microstructure, phase constituent, and mechanical properties of the as-printed samples in comparison to their as-cast counterpart, we reveal that the rapid cooling rates in AM leads to enhanced chemical homogeneity and elastic isotropy, paired with comparable mechanical properties.

Results and discussion
Minimizing defects via normalized processing diagram
Processing defects, such as pores, cracks, and un-melted particles, are common in AM metal alloys, which can significantly degrade material performance[40]. These printing defects can induce large stress concentrations and act as nucleation sites for cracks during loading that trigger premature failure[40–43]. The formation of these defects depends heavily on the heat input, cooling rate, thermal residual stresses, and feedstock material properties[40,44]. To minimize these AM defects, there are a multitude of material properties and processing parameters that need to be considered, such as laser beam power (q), scan speed (v), layer height (l), and thermal conductivity (λ). The enormous parameter space makes the analysis of printing conditions challenging. To overcome this challenge, Thomas et al. developed a powerful method to construct a normalized processing map that can inform decisions on selecting appropriate processing conditions[44]. This method normalizes the energy input per unit volume against the thermodynamic properties of a material to derive dimensionless parameters that control the peak temperature, heating rate, and minimum energy density required to fully melt a material[44]. This processing map can effectively compare and classify different processing regions to identify the effective processing window for mitigating processing defects in additively manufactured materials. In the present work, we printed a library of 28 samples with various printing conditions to explore such a processing window, as seen in Fig. 1a.

The normalized processing variables are calculated, using the following equations:

$$q^* = Aq/(r_B \lambda (T_m - T_0)) \tag{1}$$

$$v^* = v r_B / \alpha \tag{2}$$

$$l^* = 2l/r_B \tag{3}$$

$$h^* = h/r_B \tag{4}$$

In these equations, A is the laser absorptivity, r_B the laser beam radius, h the hatch spacing, λ and α the thermal conductivity and thermal diffusivity of the alloy being processed, respectively. T_m and T_0 are the melting temperature and initial temperature of the powder, respectively. q^* represents the normalized laser power, and v^* represents the normalized scan speed. They can be considered physically to control the peak temperature and heating rate induced by the laser. l^* and h^* denote the dimensionless layer thickness and hatch spacing, respectively. The volume of material heated by the laser can be approximated as $2r_B l$. According to Thomas et al.[44], the heat input per unit length can be defined as q/v. The energy per unit volume required to raise the temperature of the material to a critical temperature can be described as $q/2vlr_B$. Normalizing the energy per unit volume by the thermal conductivity and diffusivity allows us to represent this energy in dimensionless terms:

$$E^* = q^*/v^* l^* = \left[Aq/2vr_B l \right] \cdot \left[\alpha / \lambda (T_m - T_0) \right] \tag{5}$$

It should be noted that we can make the substitution, $\alpha/\lambda = 1/\rho C_p$, where ρ is the alloy density, and C_p the specific heat capacity. Although the

Fig. 1 | Sample images and corresponding processing diagram. a Image of the initial batch of as-printed TiZrNbTa cubes for process optimization. **b** Normalized processing map plotting h^* against a normalized unitless energy density required to melt the material, where the red highlighted region illustrates the effective processing window with minimized pores and un-melted particles. The red-star samples represent the samples where both the areal fractions of pores and un-melted particles are below 1%.
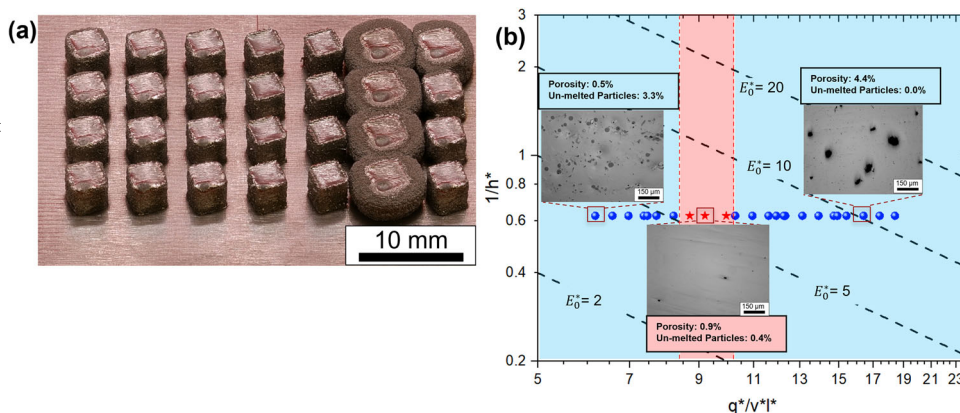
material properties are assumed to be that of the bulk material, the density can be multiplied by 0.67 to account for the powder packing on the print bed; thus, Eq. 5 can be written as:

$$E^* = q^*/v^*l^* = \left[Aq/2vr_\mathrm{B}l\right] \cdot \left[1/\left(0.67\rho C_\mathrm{p}(T_\mathrm{m} - T_0)\right)\right] \quad (6)$$

Equation 6 represents the amount of energy required in a single laser scan to raise the temperature of the powder above the melting point of the material. The minimum heat to cause melting per unit volume of material, H_min, which includes the latent heat of melting, can be written as:

$$H_\mathrm{min} = \rho C_\mathrm{p}(T_\mathrm{m} - T_0) + L_\mathrm{m} \quad (7)$$

where L_m is approximately $0.5\rho C_\mathrm{p}\Delta T$, and thus, we can substitute Eq. 7 into Eq. 6, giving:

$$E^*_\mathrm{min} = q^*/v^*l^* = \left[Aq/2vr_\mathrm{B}l\right] \cdot \left[1/\rho C_\mathrm{p}(T_\mathrm{m} - T_0)\right] \quad (8)$$

E^*_min is the unitless energy density required to melt the material. E^* can be used in conjunction with the reciprocal of normalized hatch spacing $(1/h^*)$ to produce a processing map, as seen in Fig. 1b. The material properties used in Eq. 8 are calculated by a weighted sum of the bulk properties of individual elements in the alloy composition. The reason $1/h^*$ is used is that its product with E^* gives the ratio of dimensionless volumetric heat input to dimensionless hatch spacing, which gives a factor for the normalized equivalent volumetric energy density, E^*_0. High values of E^*_0 represent combinations of parameters with excess heat input, which can lead to keyhole porosity, while low values of E^*_0 indicate inadequate heat input that can result in insufficient melting. This pattern is seen clearly in Fig. 1b, where samples with low heat inputs tend to show a high areal fraction of un-melted particles, while samples with high heat inputs tend to exhibit an increased porosity.

When using elemental powders for printing, the different elements can possess vastly different thermophysical and chemical properties (e.g., melting point, vapor pressure, laser absorptivity, heat conductivity, and oxidation resistance), thus increasing the challenge of producing defect-free samples of a desired composition, as discussed in recent review articles[35,36]. High melting-point elements like Ta and Nb require high heat inputs to melt fully. Insufficient heat input results in many un-melted particles, as observed on the left side of Fig. 1b. In contrast, the lower melting-point elements like Ti and Zr need comparatively lower heat inputs to avoid evaporation of these elements and keyholes during printing, as indicated on the right side of Fig. 1b where large keyhole pores are present. This delicate balance of the energy input suggests that only a narrow processing window can produce samples with a suitably low defect density. Within this window, a balance must be struck such that the fractions of un-melted particles and the porosity are minimized by ensuring the heat input is high enough to melt the high melting-point elements (Ta and Nb) but not overhigh that the low melting-point elements (Zr and Ti) evaporate and form keyhole pores. The red-star data points in Fig. 1b represent samples where both the areal fractions of pores and un-melted particles are below 1%, and the highlighted red region illustrates the effective processing window for achieving these high-density samples with minimized defects. It should be noted that cracking within AM RHEAs is highly related to the large thermal residual stresses caused by L-PBF[37]. In the current work, a double scanning strategy was employed, whereby each layer was scanned twice. Such a double scanning strategy has previously been shown to decrease the thermal residual stresses in as-printed parts[45,46]. The rapid cooling rates involved in additive manufacturing can induce large thermal gradients. The large thermal gradients generate significant thermal stresses that result in thermomechanical deformation and even microcracking[47]. Thus, the double scanning strategy can help mitigate cracking by reducing the thermal residual stresses in the built samples.

Mechanical properties and microstructure analysis

We used the optimized parameter set from the previous section to produce compression pillars and compared the mechanical properties of the printed TiZrNbTa RHEA (using optimized printing parameters given in the Methods section) with those of the as-cast counterpart. The true stress-strain curves of representative as-printed and as-cast samples are shown in Fig. 2a. A quantitative analysis of the stress-strain curves reveals that the as-printed sample shows a slightly higher yield strength (at 0.2% offset strain) than the as-cast sample (1187 MPa vs. 1127 MPa). The as-printed sample also exhibits more sustained work hardening than the as-cast sample. Figure 2b shows a scanning electron microscopy (SEM) image of a single melt pool in the as-printed sample where BD represents the building direction, and Fig. 2c shows an SEM image of the as-cast sample at the same magnification. While both samples exhibit a dendritic morphology, the as-printed sample exhibits significantly refined dendritic structures due to the high cooling rate ($\sim 10^6$ K/s) during L-PBF process[15,23]. Overall, the mechanical properties of the as-printed sample are slightly better but comparable to those of the as-cast counterpart despite the distinct microstructures. This comparison will be further discussed later.

Figure 3 shows the elemental distribution in both as-printed and as-cast samples. The elemental segregation in the as-cast sample is much more severe and occurs over a larger length scale than that in the as-printed sample. The as-printed sample exhibits a relatively uniform elemental

Fig. 2 | Mechanical properties and microstructures of the as-printed and as-cast samples. **a** Compressive true stress-strain curves of as-printed and as-cast TiZrNbTa RHEAs. **b** SEM image of the as-printed sample, the white dashed line illustrates the melt pool boundary. BD represents the building direction. **c** SEM image of the as-cast sample at a similar magnification.
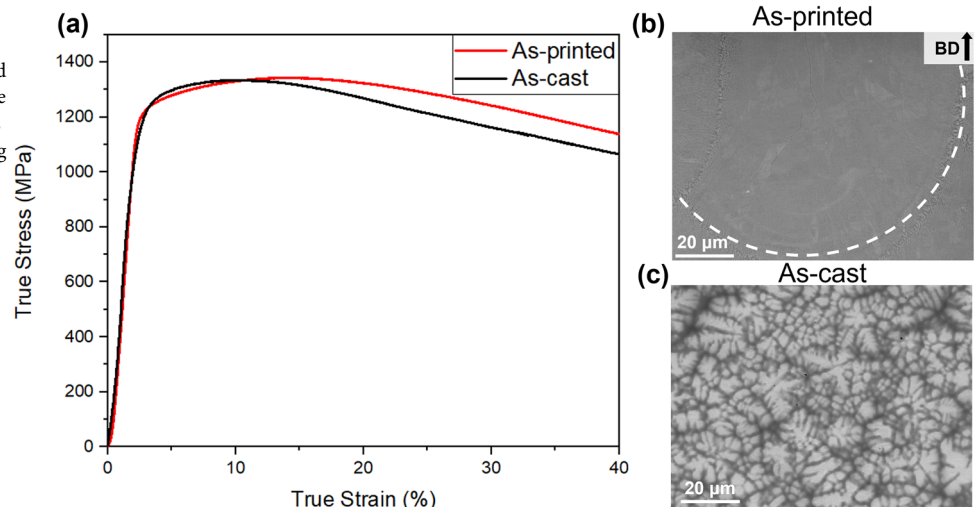
distribution within the melt pool interior with subtle elemental segregation in the heat-affected zone (HAZ) (Fig. 3a). The HAZ contains a region re-heated by subsequent build layers and neighboring laser tracks. Hence, the HAZ experiences an in-situ thermal cycling effect that promotes atomic diffusion and even solid-state phase transformation during laser AM[48–51]. The diffusion caused by cyclic heating can result in elevated chemical segregation in the HAZ versus that in the melt pool interior[52–54]. Figure 3b shows the elemental distribution in the as-cast sample, where the Ta content is highly enriched in the dendritic regions, while the Ti and Zr contents are enriched in the inter-dendritic regions. This severe chemical segregation occurs presumably due to solute ejection associated with the much lower cooling rate during the casting process.

Tables 1 and 2 summarize the chemical compositions of the dendritic and inter-dendritic regions in the as-printed and as-cast samples, respectively. In particular, Table 1 presents the chemical compositions measured in the melt pool interior and in the HAZ. The dendritic and interdendritic regions of the melt pool interior show almost no chemical segregation while the dendritic region in the HAZ is enriched in Ta and Nb, which have higher melting temperatures than Ti and Zr. The inter-dendritic region of the HAZ is slightly enriched in Ti and Zr. Table 2 reveals that the as-cast sample exhibits significant enrichment of high melting-temperature elements like Ta and Nb in the dendritic regions. Ti and Zr, which have lower melting points, are enriched in the interdendritic regions. These tables highlight the difference in chemical segregation between the dendritic and interdendritic regions in the two types of samples. These results are consistent with the elemental distribution illustrated in Fig. 3, where the as-printed sample shows a much more uniform elemental distribution while the as-cast sample presents significant segregation of the constituent elements based on their different melting points.
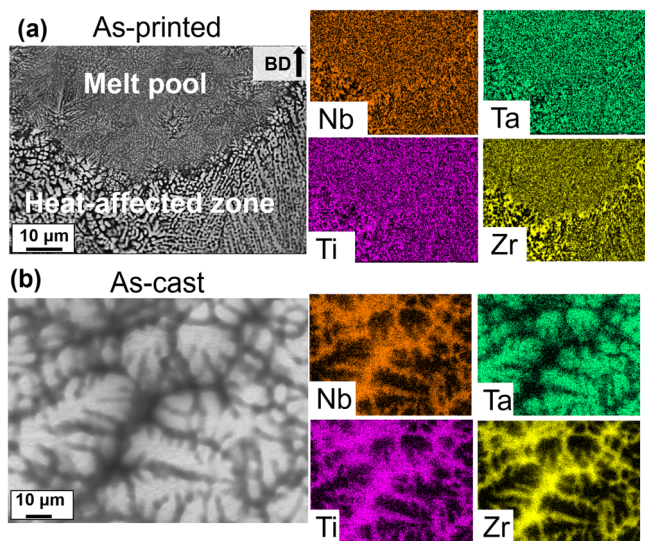

Fig. 3 | SEM and corresponding energy-dispersive X-ray spectroscopy (EDS) maps depicting the elemental segregation in each sample. a As-printed sample. BD represents the building direction. **b** As-cast sample.

We further used electron back-scatter diffraction (EBSD) to investigate the grain morphologies of both the as-printed and as-cast samples. The as-printed sample in Fig. 4a shows a heterogeneous microstructure where the large columnar grains form at the center of the melt pool while refined equiaxed grains exist at the melt pool boundary. The columnar grain structure results from the large thermal gradients established by the intensive laser heat input, leading to epitaxial grain growth from the local melt pool boundary toward the melt pool center[55,56]. The fine equiaxed grains at the melt pool boundary have also been reported in the literature[52,57,58]. In those cases, however, the precipitates containing high melting-point elements act as heterogeneous nucleation sites that encourage equiaxed grain growth at the melt pool boundary[52,57,58]. It will be noted later in the present work that the as-printed TiZrNbTa RHEA samples in our work appear to show a single-phase BCC structure. Thus, the equiaxed grain structure is not attributed to the presence of precipitates. Recall that Table 1 presents the chemical compositions of the dendritic and inter-dendritic regions in the HAZ and melt pool interior. The table demonstrates that the HAZ displays more pronounced chemical segregation, compared to the melt pool interior. In particular, we note the regions rich in Nb and Ta. Therefore, the chemical segregation at the melt pool boundary and HAZ as shown in Fig. 3a and Table 1 may lead to partial melting of some local regions with lower melting-point constituents, such as Ti and Zr during thermal cycling, while the Nb- and Ta-rich regions may act as heterogeneous nucleation sites that promote the formation of equiaxed grains at the melt pool boundary[59]. In fact, the large number of heterogeneous nucleation sites provided by such segregation at the melt pool boundary also explains the much smaller grains at the melt pool boundary versus the melt pool interior. The as-printed sample also exhibits a nearly random crystal texture throughout the entire sample with an average grain size of 14.4 μm. This random texture likely occurs due to the formation of equiaxed grains in the HAZ, which interrupts the epitaxial growth of columnar grains across layers despite the strong thermal gradients and solidification direction oriented along the build direction. In contrast, the as-cast sample displays significantly coarser equiaxed grains present throughout the entire sample (Fig. 4b). Due to the large grain sizes, an additional lower-magnification EBSD inverse pole figure (IPF) map was collected (see Supplementary Fig. 1) to allow for statistical analysis of the average grain size, which is measured to be approximately 68.2 μm. Although the microstructural morphology is very different, the as-cast sample also shows a highly random texture, which can be expected for usual suction casting conditions where the thermal gradients are significantly weaker and less directional.

**Synchrotron X-ray diffraction and neutron diffraction analysis**

In-situ synchrotron X-ray diffraction (SXRD) and in-situ neutron diffraction (ND) were employed to monitor the elastic deformation behavior, dislocation density evolution and to investigate the effect of chemical segregation on the mechanical properties of TiZrNbTa RHEAs under loading. Schematic illustrations of SXRD and ND can be found in refs. [51] and [52], respectively[60,61]. Based on Bragg's law[62], the relationship between the spacing of crystallographic lattice planes (d), the diffraction angle (2θ) of radiation that is scattered coherently through a crystalline material, and the wavelength of radiation (λ) is described as:

$$n\lambda = 2d\sin\theta \tag{9}$$

Table 1 | Chemical compositions of the dendritic and inter-dendritic regions in the as-printed sample measured by EDS

Region	Ti (at%)	Zr (at%)	Nb (at%)	Ta (at%)
Melt pool interior dendritic (bright)	26 ± 1	25 ± 1	26 ± 1	23 ± 1
Melt pool interior interdendritic (dark)	26 ± 1	26 ± 1	26 ± 1	23 ± 1
Melt pool interior overall	26 ± 1	26 ± 1	26 ± 1	23 ± 1
HAZ dendritic (bright)	22 ± 1	18 ± 2	24 ± 1	36 ± 2
HAZ inter-dendritic (dark)	27 ± 1	32 ± 2	20 ± 1	21 ± 2
HAZ overall	24 ± 1	26 ± 2	23 ± 1	27 ± 2

Table 2 | Chemical compositions of the dendritic and inter-dendritic regions in the as-cast sample measured by EDS

Region	Ti (at%)	Zr (at%)	Nb (at%)	Ta (at%)
Dendritic (bright)	21 ± 1	14 ± 1	27 ± 1	38 ± 1
Inter-dendritic (dark)	31 ± 1	38 ± 1	18 ± 1	12 ± 1
Overall	29 ± 1	27 ± 1	23 ± 1	23 ± 1

Fig. 4 | EBSD IPF maps showing the grain structure and orientation in each sample. a As-printed sample. **b** As-cast sample.

Building Direction

Loading Direction
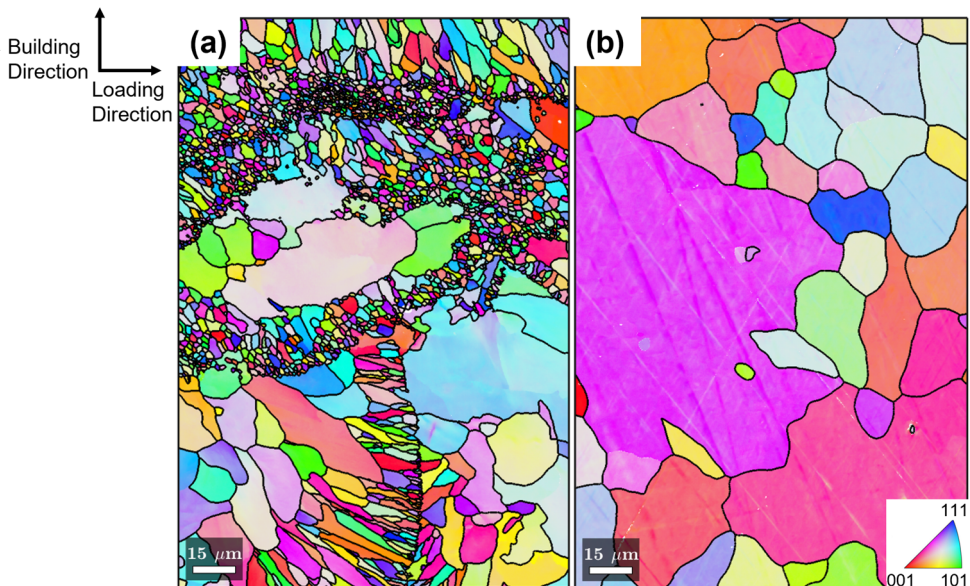
where n is the order of reflection. The crystal lattice physically acts as a natural and omni-present strain gauge embedded in each crystallite or grain[62]. To achieve high amounts of scattering, the X-rays must travel through many grains. If there are only a few grains in the path of the X-rays, many X-rays will be scattered onto individual pixels on the detector, leading to overexposure of those pixels[62]. Due to the large average grain size (68.2 μm) of the as-cast sample, it was difficult to achieve informative diffraction rings with in-situ SXRD, as the load cell was not able to accommodate a large enough sample to ensure a great number of grains being captured in the diffraction path. Hence, in-situ ND was employed to analyze the as-cast sample. ND operates using a similar Bragg's law diffraction equation but using neutrons as the incident particles rather than photons in the case of SXRD. Neutrons are scattered by the nucleus of atoms rather than the electron clouds, which result in larger mean free paths through the material[63]. This greater penetration depth ensures a larger sample size can be used without significant loss in signal strength at the detector, making ND ideal to gather data for a sample with a large grain size like the as-cast case in the current work.

Both in-situ SXRD and ND techniques allow measurements of the d-spacing of lattice planes under applied loading. The lattice strain (ε_{hkl}) evolution for both samples can be compared as:

$$\varepsilon_{hkl} = \frac{d_{hkl} - d_{0,hkl}}{d_{0,hkl}} \qquad (10)$$

where d_{hkl} is the d-spacing for a specific crystallographic plane family {hkl} under loading, and $d_{0,hkl}$ is the d-spacing of the same plane family in the load-free state. Both samples showed a BCC structure, but the as-cast sample's diffraction peaks contained significant peak splitting, suggesting that the dendritic and interdendritic regions were separate BCC phases that need to be analyzed individually (as seen in Supplementary Fig. 2). This lattice strain can be plotted for both parallel and perpendicular to the loading direction, also labeled as the axial and transverse directions, respectively. The lattice strain evolution plots in the elastic deformation regime of the as-printed and as-cast samples are presented in Fig. 5a and b, respectively. Of particular interest, we reveal that the as-printed sample exhibits higher elastic isotropy than the as-cast sample. The crystallographic lattice strains for the different crystal plane families in the as-cast sample deviate from each other significantly more than those in the as-printed sample. Previous studies have shown that the elastic isotropy of a material can influence its
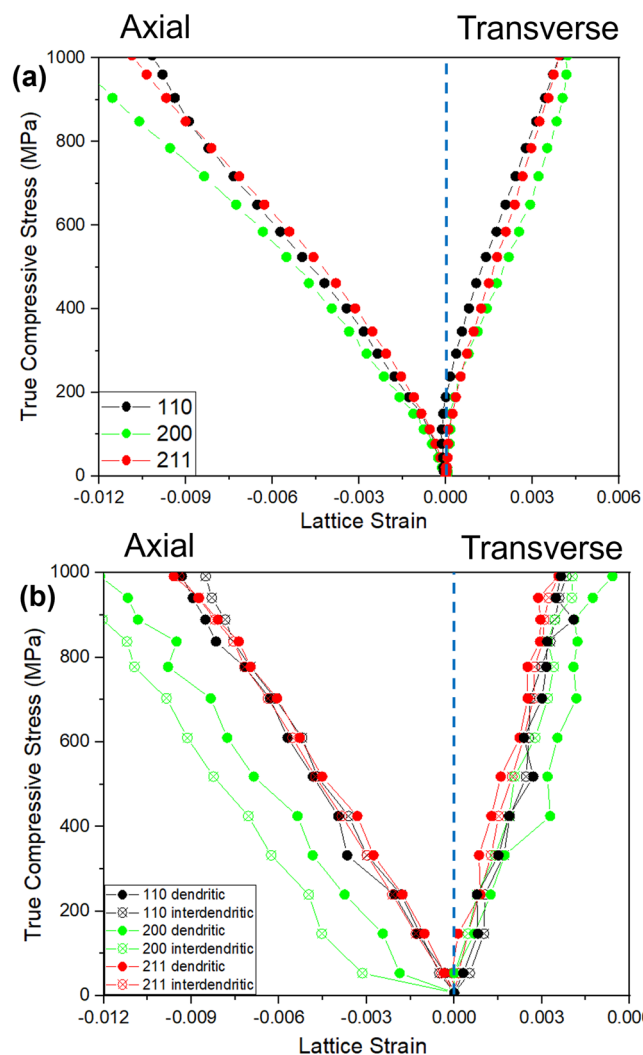

Fig. 5 | Evolution of lattice strain as a function of true applied stress. a As-printed sample. **b** As-cast sample.

Table 3 | Experimental vs. SQS supercell elastic constants of TiZrNbTa under different processing conditions

Sample region	C₁₁ (GPa)	C₁₂ (GPa)	C₄₄ (GPa)	A_z
As-cast, Dendritic (SQS)	216.7	124.4	81.2	1.75
As-cast, Dendritic (experimental)	190.3	129.1	44.7	1.47
As-cast, Inter-dendritic (SQS)	157.3	107.4	74.0	2.97
As-cast, Inter-dendritic (experimental)	179.4	124.2	43.7	1.58
As-printed (SQS)	189.4	116.6	76.3	2.09
As-printed (experimental)	164.5	118.6	31.9	1.39

plastic deformation as the grain boundary between two anisotropic grains can experience stress concentrations that reduce the material's work hardening ability[64–67]. Unraveling the different elastic properties of the as-cast and as-printed samples in the present work provides significant insight into understanding the slightly different strengthening and work-hardening behaviors between the two samples.

The isotropic behavior of both the as-printed and as-cast samples was investigated by first measuring the diffraction elastic constants (DEC) for different crystallographic plane families. These constants illustrate the elastic responses of different plane families to the macroscopic applied true stress[68]. Subsequently, these constants were used as input in the Kroner model[69] to derive the values for the single crystal elastic constants (C_{11}, C_{12}, and C_{44}) and were compared to values derived by first-principles calculations on special quasirandom structures (SQS) to verify their validity and to prove the accuracy of the calculations (see Methods). The experimental and simulated values of the elastic constants for each type of sample are shown in Table 3, along with the Zener anisotropy factor, A_z, which is calculated as $A_z = (2C_{44})/(C_{11} - C_{12})$. When A_z is close to 1, the material is more isotropic; when it is further away from 1, it is more anisotropic. From Table 3, it is seen that the as-printed sample shows substantially higher isotropic behavior. The experimental values of C_{11} and C_{12} agree well with the calculated values, but the value of C_{44} shows a large discrepancy between the simulated and experimental values. It is well-known that DFT-predicted C_{44} can have larger errors[70,71], but this error leads to a large error in A_z accordingly. Note that both the experimental and calculated A_z for the as-printed sample is closer to 1 than the average A_z of the dendritic and inter-dendritic regions of the as-cast sample (1.39 vs 1.52 for the experimental values and 2.09 vs. 2.36 for the calculated values). These results confirm that the as-printed sample exhibits enhanced elastic isotropy than the as-cast sample. The physical origin of the different elastic behaviors and a detailed discussion of the exact muffin-tin orbital coherent-potential approximation (EMTO-CPA) calculation results will be further discussed in the next section.

Machine learning analysis and theoretical elastic constants

This section presents gradient boosted tree (GBT) machine learning (ML) models, which were trained on the EMTO-CPA dataset in order to investigate the relationship between the chemical composition and universal anisotropy, A_u, of the Ti-Zr-Nb-Ta RHEA compositions. The GBT model utilized 13 estimators with a maximum depth of 6 features. Hyperparameters were tuned, using grid search with four-fold cross-validation. The model with the best hyper-parameters was tested on 20% of the dataset which was set aside for validation. The objective function used was mean squared error and the validation score was 0.007. The EMTO-CPA-calculated elastic constants for 30 different compositions are summarized in Supplementary Table 1. In Fig. 6, partial dependence plots (PDPs) (dashed orange lines), are presented along with Individual Conditional Expectation (ICE) curves (blue lines). PDPs are generated using the GBT model. The PDPs illustrate the relationship between the atomic fraction of constituent elements and the predicted A_u values of the GBT model. They illustrate how the change in the atomic fraction of a given element affects the prediction

while averaging out the effects of all other features. The ICE curves are related to PDPs in that they show how each individual data point (composition and A_u value) responds to changes in the atomic fraction of a given element. While PDPs show the average effect of a feature, ICE plots show the effect for each individual instance, providing a more detailed view. In other words, an ICE plot is an individualized version of the PDP for each observation. The small black vertical lines indicate the deciles of the data used to train the model. The combined PDP and ICE curves reveal that the addition of Nb and Ta results in the most and second most significant effects on elastic anisotropy, respectively.

Increasing the concentrations of Nb or Ta makes the RHEA more isotropic until 40 at% when the change in isotropy becomes small. Pair interactions were also analyzed using pair interaction plots, also known as two-way PDPs (Fig. 7). The two-way partial dependence plots illustrate the interaction between changes in the atomic fraction of two elements and their combined effect on the predicted A_u. The x and y axes represent atomic fractions of their respective elements, and the predicted A_u is represented by the color in the contour plot. The darker regions correspond to an average increase in elastic isotropy. As for the pair interactions, increasing Nb and Ta, increasing Nb and decreasing Ti, or increasing Nb and decreasing Zr were all found to have the strongest effects on increasing elastic isotropy. Both Figs. 6 and 7 suggest that increases in Nb and Ta contents yield enhanced elastic isotropy. However, Table 3 indicates that the dendritic region of the as-cast sample does not show more isotropic behavior than the as-printed sample despite the higher Nb and Ta contents. Previous studies have suggested that the local lattice distortions in a material can also affect the elastic isotropy/anisotropy. In particular, higher local lattice distortions have been shown to correlate with increased elastic isotropy[72], large micro-scale residual stresses can also influence lattice distortions[73]. As previously mentioned, laser-based AM techniques result in extremely high cooling rates which can induce significant thermal residual stresses. Thus, the improved isotropic behavior of the as-printed sample may also arise from the large residual stresses. These results suggest that AM opens up a unique opportunity to further tune elastic properties of a material by precisely controlling thermal history of the sample to vary the residual stresses in the as-printed part.

Strengthening mechanisms

This section presents the theoretical calculations and estimated contributions of different strengthening mechanisms that lead to the slightly different yield strengths of the two types of samples. In the case of single-phase solid solution RHEAs, there are essentially three main strengthening mechanisms that contribute to the yield strength; these are solid solution hardening (σ_{SSH}), dislocation hardening (σ_ρ), and grain-boundary strengthening (σ_{HP}). Thus, the yield strength is estimated as follows:

$$\sigma_y = \sigma_f + \sigma_{SSH} + \sigma_\rho + \sigma_{HP} \qquad (11)$$

where σ_y is the yield strength, and σ_f is the lattice friction of the alloy. The solid solution hardening is known to be difficult to calculate for near equiatomic HEAs as there is no clear solute or solvent atoms[74]. Zhao et al. previously estimated the combined strengthening contribution of lattice friction and solid solution for the TiZrNbTa equiatomic alloy as approximately 826 MPa[75].

The dislocation strengthening can be calculated based on the Taylor hardening law:

$$\sigma_\rho = M\alpha Gb\rho^{1/2} \qquad (12)$$

where $M = 3.1$, for both samples, is the Taylor factor measured from EBSD. $\alpha \approx 0.3$ is a geometric constant [29], G is the shear modulus, b is the Burgers vector, and ρ is the dislocation density. The dislocation density is calculated by using the modified Williamson-Hall analysis method[76]. By combining the previously mentioned quantities into Eq. 12, we can calculate the Taylor strengthening values for the as-printed and as-cast samples as 269 MPa and

Fig. 6 | Combined PDP and ICE plots for each element in the Ti-Zr-Nb-Ta RHEA system. a PDP and ICE plot for Nb. **b** PDP and ICE plot for Ta. **c** PDP and ICE plot for Zr. **d** PDP and ICE plot for Ti.
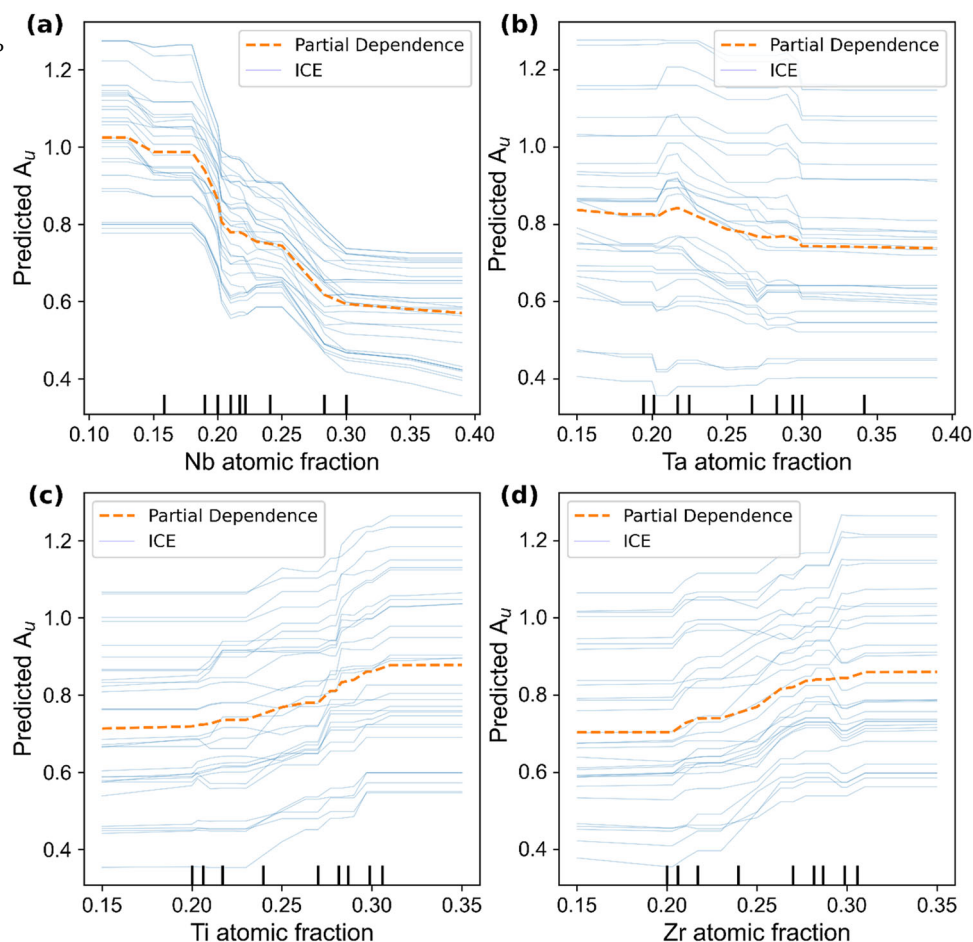
169 MPa, respectively. Figure 8 shows the evolution of dislocation density as a function of the true strain. The as-printed sample shows a higher dislocation density than both the dendritic and inter-dendritic regions of the as-cast sample. Also, the dislocation density in the as-printed sample increases much faster than that in the as-cast sample, which explains the generally higher work hardening rate observed for the as-printed sample in Fig. 2a. The increased dislocation density is also confirmed via measurements of the kernel average misorientation (KAM) of both samples at 5%, 10%, and 20% true strains. EBSD KAM maps are presented in Supplementary Fig. 3. A quantitative analysis of the average KAM values is presented in Supplementary Fig. 4, which displays that the as-printed sample exhibits a higher average KAM value at each respective strain level. Note that the KAM value is proportional to the geometrically necessary dislocation (GND) density but does not account for the statistically stored dislocations (SSD) and is sensitive to the step size used during EBSD. Thus, the EBSD KAM data only serves as a relative measure of the dislocation density between the two types of samples.

Finally, the grain-boundary strengthening is estimated by the Hall-Petch (H-P) relationship:

$$\sigma_{\mathrm{HP}} = k_{\mathrm{HP}} d^{-1/2} \tag{13}$$

where $k_{\mathrm{HP}} \approx 240 \, MPa \cdot \mu m^{1/2}$ is the Hall-Petch coefficient [30], and d is the grain size. The average grain size was measured by EBSD as 14.4 μm for the as-printed sample and 68.2 μm for the as-cast sample. To ensure a statistically significant number of grains was used to measure the grain size in the as-cast sample, a lower magnification EBSD scan was carried out (see Supplementary Fig. 1). Using the measured grains sizes, the H-P strengthening value for the as-printed and as-cast samples is estimated as

63 MPa and 23 MPa, respectively. Combining the contribution from each strengthening mechanism, we can estimate the expected yield strength for each sample. Figure 9 shows the plots of the theoretically estimated yield strength, compared to the experimentally measured yield strength. The estimated yield strengths of both samples show good agreement with the experimentally measured values within 10% deviations. The as-printed material shows a slightly better match than the as-cast material. These calculations also highlight that the slight increase in yield strength for the as-printed sample originates primarily from the smaller grain size and higher dislocation density, which are both rooted in the rapid cooling during L-PBF compared to casting.

Conclusions
In this study, we present a method to produce an equiatomic TiZrNbTa RHEA by in situ alloying using elemental powders of Ti, Zr, Nb, and Ta during L-PBF. Through a normalized model-based processing diagram, we identify an effective processing window that accounts for both the energy input and thermophysical properties of this alloy toward mitigation of processing defects, such as porosity and un-melted powders, resulting in an alloy that is defect-less. The as-printed alloy shows substantially enhanced elastic isotropy and slightly mechanical properties compared to its as-cast counterpart. The high cooling rate during L-PBF leads to a significantly smaller grain size, higher dislocation density, and decreased chemical segregation, compared to the as-cast counterpart. A detailed analysis of the microstructures and mechanical properties provides insights into the origin of the yield strengths of the two types of samples. In particular, the smaller grain size and higher dislocation density of the additively manufactured TiZrNbTa give rise to a slightly higher yield strength, while the reduced chemical segregation results in more elastic isotropy that promotes the
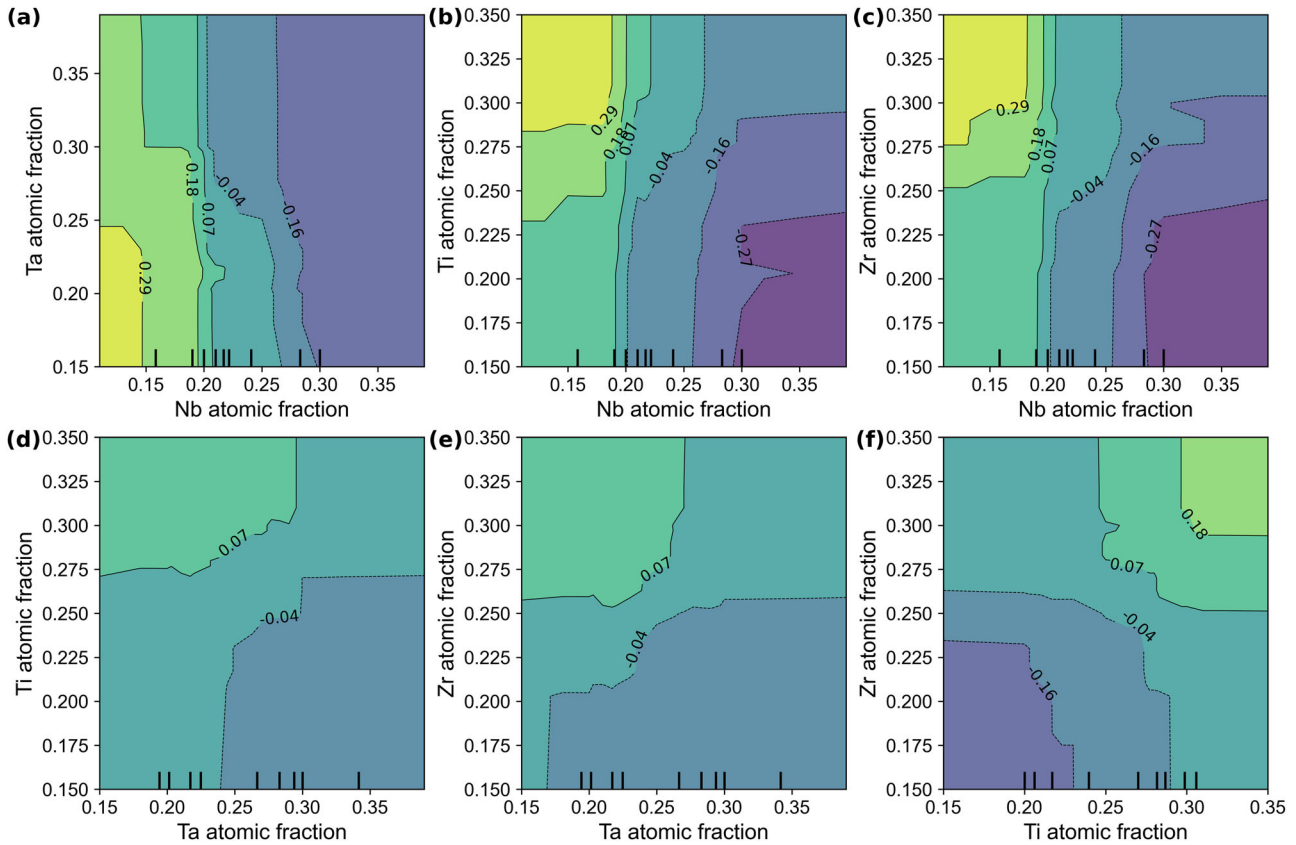
Fig. 7 | Two-way PDP plots of elemental pairs for Ti-Zr-Nb-Ta RHEA system. a Two-way PDP plot of Ta and Nb. **b** Two-way PDP plot of Ti and Nb. **c** Two-way PDP plot of Zr and Nb. **d** Two-way PDP plot of Ti and Ta. **e** Two-way PDP plot of Zr and Ta. **f** Two-way PDP plot of Zr and Ti.
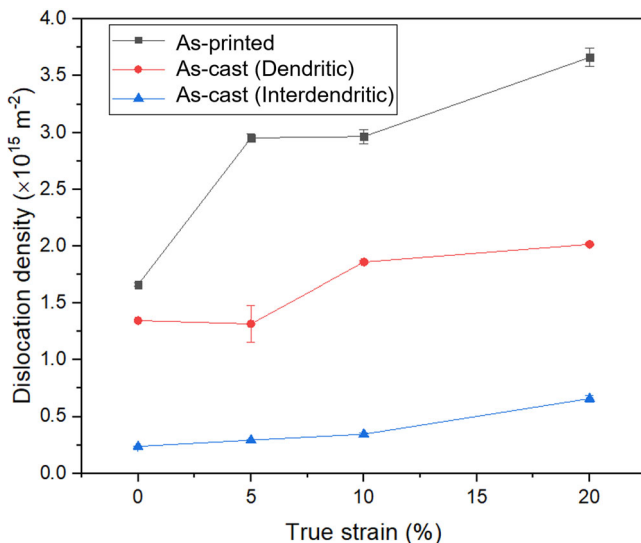

Fig. 8 | Dislocation density evolution in different samples and regions. The dislocation density was calculated via the modified Williamson-Hall analysis, where the error bars represent the mean square error of the analysis.

Fig. 9 | Comparison of experimentally measured yield strength and theoretically calculated yield strength. Calculations were based on contributions of different strengthening mechanisms.

defect-less multi-component refractory alloys without the need for investing in prohibitively expensive pre-alloyed refractory powders.

Methods
Sample fabrication
Gas-atomized elemental powders of Ti, Nb, Zr, and Ta (purity > 99.5%) with a size range of 15–60 μm were mixed in an equiatomic ratio using a Turbula mixer for 3 hours. EDS mapping was conducted on the mixed powders to ensure that powders were thoroughly mixed (Fig. 10). An initial library consisting of many 3 mm × 3 mm × 3 mm cubic samples was printed on a Ti substrate with different printing parameters by an EOS M290 L-PBF

work-hardening ability. In-depth analysis of the deformation behaviors of both materials also reveals that the improved work-hardening capability of the as-printed sample allows it to accommodate dislocation multiplication during deformation compared to the as-cast sample. Through leveraging the high cooling rate and in situ alloying capabilities of L-PBF, the present work presents an opportunity for cost-effective printing of
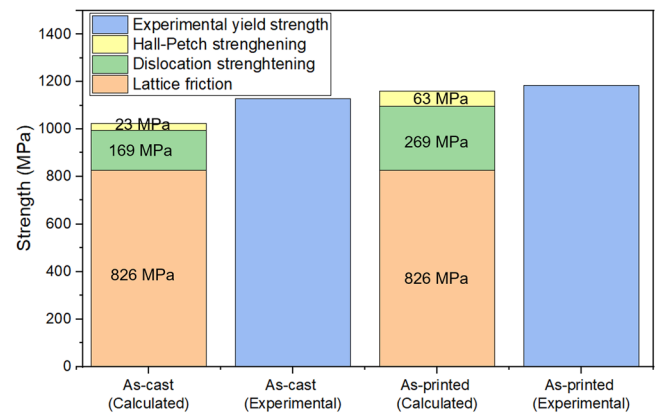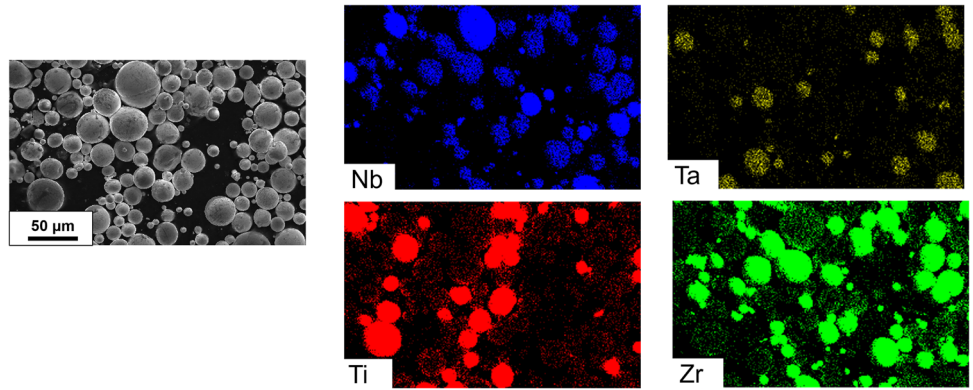
Fig. 10 | EDS maps of the mixed elemental powders. The elemental powders are mixed uniformly prior to laser additive manufacturing.

system to identify the effective processing window (Fig. 1). This L-PBF printer has an ytterbium-fiber laser with a wavelength ranging from 1060 nm to 1100 nm and a focal beam width of 100 µm. The printing chamber was purged with argon to reduce the environmental oxygen concentration to below 1000 ppm to protect the samples from oxidation during printing. The hatch spacing and layer height were held constant at 80 µm and 40 µm, respectively. The laser power and scanning speed were varied in the ranges of 300–370 W and 400–1000 mm/s, respectively. In the present work, a double scanning strategy was used, whereby each layer was scanned twice by the laser (using the same printing parameters for the first and second scan) to promote alloying of the elemental powders. Plate-shaped samples of 4 mm × 10 mm × 3 mm were then printed with the optimized printing parameters (laser power of 370 W, scan speed of 800 mm/s). For comparison, cast samples were fabricated by arc-melting a mixture of Ti, Nb, Zr, and Ta pure elements (purity > 99.95 wt%) in a Ti-gettered argon atmosphere. The ingots were re-melted ten times to ensure chemical homogeneity before suction casting into a water-cooled copper hearth with a rectangular cross-section of 4 mm × 12 mm. The as-cast plate has dimensions of 4 mm × 12 mm × 32 mm.

Mechanical testing

Compression pillars of 2 mm × 2 mm × 4 mm were cut from both the as-cast and as-printed samples using wire electric discharge machining. Uni-axial compression tests were conducted at a strain rate of 2×10^{-4} s^{-1} on an Instron 5969 machine with a built-in laser extensometer to measure the strain precisely.

Material characterization

Samples were mechanically polished using 400, 600, 800, and 1200 grit sandpapers, followed by polishing with 1-µm diamond suspension solution and 20-nm colloidal silica solution. The porosity and areal fraction of the un-melted powders in the as-printed samples were analyzed using images taken by an optical microscope (OM, OLYMPUS SC50) and processed in ImageJ software. Microstructure characterization was performed using the Thermo Scientific Scios 2 DualBeam SEM, coupled with the symmetry EBSD detector (Oxford lnc.). The EBSD acquisitions were performed using a 6.4 nA current at an accelerating voltage of 20 kV, scanning a 1002×688 pixel grid on the surface of the sample with a 0.2 µm measurement step size. Post-processing and visualization of the EBSD data were obtained utilizing the MTEX package (v. 5.8.1)[77]. The misorientation angle criteria were used to categorize grain-boundaries character—with misorientation angles 15—62.5° categorized as high-angle grain boundaries (HAGBs). The Kernel Average Misorientation (KAM) maps were constructed, based on the average disorientation between a given point in the scan and its neighbors ($n = 2$), and 5° threshold angle. Chemical composition analysis was performed, using a Magellan 400 XHR-SEM equipped with an Oxford EDS detector operated at a voltage of 20 kV. In-situ compression SXRD was performed on the as-printed sample during

compression at the 11-ID-C synchrotron X-ray source at the Argonne National Laboratory (ANL). For the SXRD experiment, square pillar samples with dimensions of $1.3 \times 1.3 \times 2.6$ mm were used. In-situ ND was performed on the as-cast samples at VULCAN BL-7 at the spallation neutron source (SNS), oak ridge national laboratory (ORNL). Cylindrical compression pillars with a diameter of 6 mm and a height of 15 mm were used for neutron diffraction.

First-principles calculations and machine-learning modeling

High-throughput first-principles calculations were performed using the exact muffin-tin orbital coherent-potential approximation (EMTO-CPA) method to screen the TiZrNbTa RHEA compositional space[78,79]. These calculations help us understand the effect of composition on the elastic properties. Through correlating the elastic properties with the chemical composition, we aim to understand how chemical segregation between the dendritic and interdendritic regions in the samples affect the elastic properties. The lattice and elastic constants of 30 compositions were calculated to map the compositional effect on the mechanical properties of the TiZrNbTa RHEA. The compositions chosen had one to three constituent elemental concentrations deviating from the equimolar concentration in small increments with a maximum deviation of 14 at%. The energy, E, vs. volume, V, pairs were used to fit the Birch-Murnaghan equation of state (EOS)[79] in Eq. 14, where E_0, and V_0, are the equilibrium energy and volume, respectively. B'_0 is the derivative of the bulk modulus with respect to pressure. The bulk modulus, B_0, is obtained from the EOS.

$$E(V) = E_0 + \frac{9V_0 B_0}{16}\left\{ \left[\left(\frac{V_0}{V} \right)^{\frac{2}{3}} - 1 \right]^3 B'_0 + \left[\left(\frac{V_0}{V} \right)^{\frac{2}{3}} - 1 \right]^2 \left[6 - 4\left(\frac{V_0}{V} \right)^{\frac{2}{3}} \right] \right\}$$

(14)

Next, the elastic constants for each composition were found by fitting energy changes to deformed lattices. The amount of orthorhombic deformation defined in Eq. 15 is fit to energy changes to obtain tetragonal shear modulus, c', Eq. 16. Elastic constants, C_{11} and C_{12}, were derived using Eqs. 17 and 18. The change in energy due to monoclinic deformation, Eq. 19, was fit in Eq. 20 to obtain the C_{44} elastic constant.

$$\mathscr{D}_t + \mathscr{I} = \begin{pmatrix} 1 + \delta_o & 0 & 0 \\ 0 & 1 - \delta_o & 0 \\ 0 & 0 & \frac{1}{1 - \delta_o{}^2} \end{pmatrix}$$

(15)

$$\triangle E(\delta_o) = 2Vc'\,\delta_o^2 + \mathcal{O}(\delta_o^4)$$

(16)

$$B = \frac{(C_{11} + 2C_{12})}{3}$$

(17)

$$c' = \frac{(C_{11} - C_{12})}{2} \tag{18}$$

$$\mathscr{D}_{\mathrm{m}} + \mathscr{I} = \begin{pmatrix} 1 & \delta_{\mathrm{m}} & 0 \\ \delta_{\mathrm{m}} & 1 & 0 \\ 0 & 0 & \frac{1}{1-\delta_{\mathrm{m}}^2} \end{pmatrix} \tag{19}$$

$$\triangle E(\delta_{\mathrm{m}}) = 2VC_{44}\delta_{\mathrm{m}}^2 + \mathscr{O}(\delta_{\mathrm{m}}^4) \tag{20}$$

The aggregate elastic moduli were then calculated, using Eqs. 21–25. We used the arithmetic Hill average for the calculated aggregate shear modulus: $G = \frac{G_{\mathrm{V}} + G_{\mathrm{R}}}{2}$, where G_{V} is the Voigt bound Eq. 21 and G_{R} is the Reuss bound Eq. 22. The Young's modulus E and Poisson's ratio ν were obtained from Eq. 23 and Eq. 24, respectively. The universal anisotropy ratio is given by A_{u} in Eq. 25[80]. An elastically isotropic crystal has an A_{u} value of 0.

$$G_{\mathrm{V}} = \frac{C_{11} - C_{12} + 3C_{44}}{5} \tag{21}$$

$$G_{\mathrm{R}} = \frac{5(C_{11} - C_{12})C_{44}}{4C_{44} + 3(C_{11} - C_{12})} \tag{22}$$

$$E = \frac{9BG}{3B + G} \tag{23}$$

$$\nu = \frac{3B - 2G}{2(3B + G)} \tag{24}$$

$$A_{\mathrm{u}} = 5\frac{G^{\mathrm{V}}}{G^{\mathrm{R}}} + \frac{K^{\mathrm{V}}}{K^{\mathrm{R}}} - 6 \tag{25}$$

Then, a gradient-boosted trees (GBT) machine learning model was trained, employing the elemental concentrations as features, and A_{u} as the target. The GBT model was utilized to analyze the effect of changing the concentration of a single element as well as pair interactions on A_{u}.

More accurate planewave density functional theory (DFT) calculations were performed to calculate elastic constants of the experimentally measured compositions in the dendritic and interdendritic regions. These first-principles calculations were performed, using the Vienna ab-initio simulation package (VASP) to calculate the single-crystal elastic constants[81,82] based on the projector augmented wave (PAW) method[83]. The exchange-correlation energy was described with the generalized gradient approximation (GGA) in the Perdew–Becke–Ernzehof (PBE) parameterization[84]. A plane-wave cutoff of 520 eV and gamma-centered k-point meshes with a density of 5000 k-points per reciprocal atom were used. All structures were optimized until the energy was converged within 10^{-5} eV per supercell. The chemical disorder was modeled with special quasirandom structures (SQS)[85]. The SQS were generated, using the Monte Carlo SQS code from the Alloy Theoretic Automated Toolkit (ATAT), which uses a Monte Carlo algorithm with an objective function to find the closest match of correlation functions of a disordered state[86]. The convergence of elastic constants was tested with a series of SQS with different sizes.

The elastic tensor was calculated using a computational workflow based on the stress-strain method described in ref. 71. Starting with a relaxed SQS of the HEA, a set of distorted structures were generated using 3×3 Green-Lagrange strain tensors of varying magnitudes at ±0.5% and ±1%. For each distorted structure, the 3×3 stress tensor is computed by DFT. The elastic tensor of the SQS is calculated from the relationship between the stress and strain tensors.

Data availability
The data that support the findings of this study are available from the corresponding author upon reasonable request.

References
1. Blakey-Milner, B. et al. Metal additive manufacturing in aerospace: a review. *Mater. Des.* **209**, 110008 (2021).
2. Yu, W. et al. Processing and characterization of crack-free 7075 aluminum alloys with elemental Zr modification by laser powder bed fusion. *Mater. Sci. Add. Manuf.* **1**, 4 (2022).
3. Frazier, W. E. Metal additive manufacturing: a review. *J. Mater. Eng. Perform.* **23**, 1917–1928 (2014).
4. Pantawane, M. V., Ho, Y.-H., Joshi, S. S. & Dahotre, N. B. Computational assessment of thermokinetics and associated microstructural evolution in laser powder bed fusion manufacturing of Ti6Al4V alloy. *Sci. Rep.* **10**, 7579 (2020).
5. Pantawane, M. V., Dasari, S., Mantri, S. A., Banerjee, R. & Dahotre, N. B. Rapid thermokinetics driven nanoscale vanadium clustering within martensite laths in laser powder bed fused additively manufactured Ti6Al4V. *Mater. Res. Lett.* **8**, 383–389 (2020).
6. Pantawane, M. V. et al. Coarsening of martensite with multiple generations of twins in laser additively manufactured Ti6Al4V. *Acta Mater.* **213**, 116954 (2021).
7. Kenel, C. et al. In situ investigation of phase transformations in Ti-6Al-4V under additive manufacturing conditions combining laser melting and high-speed micro-X-ray diffraction. *Sci. Rep.* **7**, 16358 (2017).
8. Li, C., Liu, Z. Y., Fang, X. Y. & Guo, Y. B. Residual stress in metal additive manufacturing. *Procedia CIRP* **71**, 348–353 (2018).
9. Wang, Y. M. et al. Additively manufactured hierarchical stainless steels with high strength and ductility. *Nat. Mater.* **17**, 63–71 (2018).
10. Kumara, C., Balachandramurthi, A. R., Goel, S., Hanning, F. & Moverare, J. Toward a better understanding of phase transformations in additive manufacturing of Alloy 718. *Mater.* **13**, 100862 (2020).
11. Chen, W. et al. Microscale residual stresses in additively manufactured stainless steel. *Nat. Commun.* **10**, 4338 (2019).
12. Ostovari Moghaddam, A., Shaburova, N. A., Samodurova, M. N., Abdollahzadeh, A. & Trofimov, E. A. Additive manufacturing of high entropy alloys: A practical review. *J. Mater. Sci. Technol.* **77**, 131–162 (2021).
13. George, E. P., Raabe, D. & Ritchie, R. O. High-entropy alloys. *Nat. Rev. Mater.* **4**, 515–534 (2019).
14. Guan, S. et al. Additive manufacturing of high-entropy alloys: microstructural metastability and Mechanical behavior. *Mecha Behav. J. Phase Equilib. Diffus.* **42**, 748–771 (2021).
15. Liu, Y. et al. Microstructure and mechanical behavior of additively manufactured CoCrFeMnNi high-entropy alloys: Laser directed energy deposition versus powder bed fusion. *Acta Mater.* **250**, 118884 (2023).
16. Chua, C., Sing, S. L. & Chua, C. K. Characterisation of in-situ alloyed titanium-tantalum lattice structures by laser powder bed fusion using finite element analysis. *Virt. Phys. Prototyp.* **18**, e2138463 (2023).
17. Zhang, X. et al. Influence of erbium addition on the defects of selective laser-melted 7075 aluminium alloy. *Virt. Phys. Prototyp.* **17**, 406–418 (2022).
18. Senkov, O. N., Miracle, D. B., Chaput, K. J. & Couzinie, J.-P. Development and exploration of refractory high entropy alloys—A review. *J. Mater. Res.* **33**, 3092–3128 (2018).
19. Senkov, O. N., Jensen, J. K., Pilchak, A. L., Miracle, D. B. & Fraser, H. L. Compositional variation effects on the microstructure and properties of a refractory high-entropy superalloy AlMo0.5NbTa0.5TiZr. *Mater. Des.* **139**, 498–511 (2018).
20. Gludovatz, B. et al. A fracture-resistant high-entropy alloy for cryogenic applications. *Science* **345**, 1153–1158 (2014).
21. Jin, X., Zhou, Y., Zhang, L., Du, X. & Li, B. A novel Fe 20 Co 20 Ni 41 Al 19 eutectic high entropy alloy with excellent tensile properties. *Mater. Lett.* **216**, 144–146 (2018).

22. Ai, C. et al. Alloy design, micromechanical and macromechanical properties of CoCrFeNiTax eutectic high entropy alloys. *J. Alloy. Compd.* **735**, 2653–2662 (2018).

23. Ren, J. et al. Strong yet ductile nanolamellar high-entropy alloys by additive manufacturing. *Nature* **608**, 62–68 (2022).

24. Ouyang, D. et al. High-strength lamellar high-entropy alloys in-situ synthesized by laser additive manufacturing. *Mater. Sci. Eng.: A* **867**, 144745 (2023).

25. Moschetti, M. et al. Design considerations for high entropy alloys in advanced nuclear applications. *J. Nucl. Mater.* **567**, 153814 (2022).

26. Dobbelstein, H., Gurevich, E. L., George, E. P., Ostendorf, A. & Laplanche, G. Laser metal deposition of a refractory TiZrNbHfTa high-entropy alloy. *Addit. Manuf.* **24**, 386–390 (2018).

27. Dobbelstein, H., Gurevich, E. L., George, E. P., Ostendorf, A. & Laplanche, G. Laser metal deposition of compositionally graded TiZrNbTa refractory high-entropy alloys using elemental powder blends. *Addit. Manuf.* **25**, 252–262 (2019).

28. Nguyen, V. T. et al. A novel quaternary equiatomic Ti-Zr-Nb-Ta medium entropy alloy (MEA). *Intermetallics* **101**, 39–43 (2018).

29. Dirras, G. et al. Elastic and plastic properties of as-cast equimolar TiHfZrTaNb high-entropy alloy. *Mater. Sci. Eng.: A* **654**, 30–38 (2016).

30. Hou, P. et al. Effect of build height on temperature evolution and thermally induced residual stresses in plasma arc additively manufactured stainless steel. *Metall. Mater. Trans. A* **53**, 627–639 (2022).

31. Talignani, A. et al. A review on additive manufacturing of refractory tungsten and tungsten alloys. *Addit. Manuf.* **58**, 103009 (2022).

32. Zhang, X. et al. Microstructure evolution and performance enhancement of NbTaTiV-(Cr, Zr, W) single-phase refractory high-entropy alloy coatings: role of additional elements. *J. Alloy. Compd.* **951**, 169918 (2023).

33. Wang, H. et al. In situ X-ray and thermal imaging of refractory high entropy alloying during laser directed deposition. *J. Mater. Process. Technol.* **299**, 117363 (2022).

34. Melia, M. A. et al. High-throughput additive manufacturing and characterization of refractory high entropy alloys. *Appl. Mater. Today* **19**, 100560 (2020).

35. Sing, S. L. et al. Emerging metallic systems for additive manufacturing: In-situ alloying and multi-metal processing in laser powder bed fusion. *Prog. Mater. Sci.* **119**, 100795 (2021).

36. Mosallanejad, M. H., Niroumand, B., Aversa, A. & Saboori, A. In-situ alloying in laser-based additive manufacturing processes: a critical review. *J. Alloy. Compd.* **872**, 159567 (2021).

37. Gu, P., Qi, T., Chen, L., Ge, T. & Ren, X. Manufacturing and analysis of VNbMoTaW refractory high-entropy alloy fabricated by selective laser melting. *Int. J. Refract. Met. Hard Mater.* **105**, 105834 (2022).

38. Li, Q. et al. Comparative study of the microstructures and mechanical properties of laser metal deposited and vacuum arc melted refractory NbMoTa medium-entropy alloy. *Int. J. Refract. Met. Hard Mater.* **88**, 105195 (2020).

39. Chen, Y. et al. In-situ Synchrotron imaging of keyhole mode multi-layer laser powder bed fusion additive manufacturing. *Appl. Mater. Today* **20**, 100650 (2020).

40. Mooraj, S., Dong, J., Xie, K. Y. & Chen, W. Formation of printing defects and their effects on mechanical properties of additively manufactured metal alloys. *J. Appl. Phys.* **132**, 225108 (2022).

41. Cunningham, R. et al. Keyhole threshold and morphology in laser melting revealed by ultrahigh-speed x-ray imaging. *Science* **363**, 849–852 (2019).

42. Zhao, Y., Ma, Z., Yu, L. & Liu, Y. New alloy design approach to inhibiting hot cracking in laser additive manufactured nickel-based superalloys. *Acta Mater.* **247**, 118736 (2023).

43. Lee, Y. et al. Transformation-induced plasticity in the heterogeneous microstructured Ti-Zr-Nb-Sn alloy via in-situ alloying with directed energy deposition. *Addit. Manuf.* **58**, 102990 (2022).

44. Thomas, M., Baxter, G. J. & Todd, I. Normalised model-based processing diagrams for additive layer manufacture of engineering alloys. *Acta Mater.* **108**, 26–35 (2016).

45. Chen, C., Xiao, Z., Wang, Y., Yang, X. & Zhu, H. Prediction study on in-situ reduction of thermal stress using combined laser beams in laser powder bed fusion. *Addit. Manuf.* **47**, 102221 (2021).

46. Luo, Y., Wang, M., Tu, J., Jiang, Y. & Jiao, S. Reduction of residual stress in porous Ti6Al4V by in situ double scanning during laser additive manufacturing. *Int. J. Miner. Metall. Mater.* **28**, 1844–1853 (2021).

47. Qian, D. et al. Statistical study of ductility-dip cracking induced plastic deformation in polycrystalline laser 3D printed Ni-based superalloy. *Sci. Rep.* **7**, 2859 (2017).

48. Chen, S. et al. Effect of solid-state phase transformation on residual stress of selective laser melting Ti6Al4V. *Mater. Sci. Eng.: A* **819**, 141299 (2021).

49. Zhang, M. et al. Additive manufacturing of in-situ strengthened dual-phase AlCoCuFeNi high-entropy alloy by selective electron beam melting. *J. Alloy. Compd.* **893**, 162259 (2022).

50. Wu, Y., Zhang, S., Cheng, X. & Wang, H. Investigation on solid-state phase transformation in a Ti-47Al-2Cr-2V alloy due to thermal cycling during laser additive manufacturing process. *J. Alloy. Compd.* **799**, 325–333 (2019).

51. Kirka, M. M., Nandwana, P., Lee, Y. & Dehoff, R. R. Solidification and solid-state transformation sciences in metals additive manufacturing. *Scr. Mater.* **135**, 130–134 (2017).

52. Okugawa, M., Ohigashi, Y., Furushiro, Y., Koizumi, Y. & Nakano, T. Equiaxed grain formation by intrinsic heterogeneous nucleation via rapid heating and cooling in additive manufacturing of aluminum-silicon hypoeutectic alloy. *J. Alloy. Compd* **919**, 165812 (2022).

53. Ng, C. H., Bermingham, M. J. & Dargusch, M. S. Eliminating segregation defects during additive manufacturing of high strength β-titanium alloys. *Addit. Manuf.* **39**, 101855 (2021).

54. Xiao, W., Xu, Y., Xiao, H., Li, S. & Song, L. Investigation of the Nb element segregation for laser additive manufacturing of nickel-based superalloys. *Int. J. Heat Mass Transfer* **180**, 121800 (2021).

55. Paul, S. et al. A discrete dendrite dynamics model for epitaxial columnar grain growth in metal additive manufacturing with application to Inconel. *Addit. Manuf.* **36**, 101611 (2020).

56. Liu, J. & To, A. C. Quantitative texture prediction of epitaxial columnar grains in additive manufacturing using selective laser melting. *Addit. Manuf.* **16**, 58–64 (2017).

57. Liu, P. et al. Insight into the mechanisms of columnar to equiaxed grain transition during metallic additive manufacturing. *Addit. Manuf.* **26**, 22–29 (2019).

58. Thapliyal, S. et al. Design of heterogeneous structured Al alloys with wide processing window for laser-powder bed fusion additive manufacturing. *Addit. Manuf.* **42**, 102002 (2021).

59. Liu, Y. et al. Additive manufacturing of high strength copper alloy with heterogeneous grain structure through laser powder bed fusion. *Acta Mater.* **220**, 117311 (2021).

60. Liu, T. K. et al. Interface coherency strain relaxation due to plastic deformation in single crystal Ni-base superalloys. *Mater. Sci. Eng.: A* **568**, 83–87 (2013).

61. An, K., Chen, Y. & Stoica, A. D. VULCAN: A "hammer" for high-temperature materials research. *MRS Bull.* **44**, 878–885 (2019).

62. Withers, P. J. Synchrotron X-ray Diffraction. in *Practical Residual Stress Measurement Methods* (ed. Schajer, G. S.) 163–194 (John Wiley & Sons, Ltd, 2013). https://doi.org/10.1002/9781118402832.ch7.

63. Lovesey, S. W. *Theory of neutron scattering from condensed matter.* (Clarendon Press, 1984).

64. Meric De Bellefon, G. & Van Duysen, J. C. Finite element analysis of the influence of elastic anisotropy on stress intensification at stress

corrosion cracking initiation sites in fcc alloys. *J. Nucl. Mater.* **503**, 22–29 (2018).

65. Ye, Y. X. et al. Evaluating elastic properties of a body-centered cubic NbHfZrTi high-entropy alloy – A direct comparison between experiments and ab initio calculations. *Intermetallics* **109**, 167–173 (2019).

66. Raturi, A., Biswas, K. & Gurao, N. P. Elastic and plastic anisotropy in a refractory high entropy alloy utilizing combinatorial instrumented indentation and electron backscatter diffraction. *J. Alloy. Compd.* **896**, 162902 (2022).

67. Feng, R. et al. Elastic behavior of binary and ternary refractory multi-principal-element alloys. *Mater. Des.* **219**, 110820 (2022).

68. Sparks, T. et al. Mechanical characterisation of V-4Cr-4Ti alloy: tensile tests under high energy synchrotron diffraction. *J. Nuclear Mater.* **569**, 153911 (2022).

69. Wang, Z., Stoica, A. D., Ma, D. & Beese, A. M. Diffraction and single-crystal elastic constants of Inconel 625 at room and elevated temperatures determined by neutron diffraction. *Mater. Sci. Eng.: A* **674**, 406–412 (2016).

70. Zhang, J., Cai, C., Kim, G., Wang, Y. & Chen, W. Composition design of high-entropy alloys with deep sets learning. *npj Comput Mater.* **8**, 89 (2022).

71. De Jong, M. et al. Charting the complete elastic properties of inorganic crystalline compounds. *Sci Data* **2**, 150009 (2015).

72. Meng, H. et al. Influence of local lattice distortion on elastic properties of hexagonal close-packed TiZrHf and TiZrHfSc refractory alloys. *Phys. Status Solidi B* **258**, 2100025 (2021).

73. Yu, D., An, K., Chen, X. & Bei, H. Phase-specific deformation behavior of a NiAl–Cr(Mo) lamellar composite under thermal and mechanical loads. *J. Alloy. Compd.* **656**, 481–490 (2016).

74. Senkov, O. N., Scott, J. M., Senkova, S. V., Miracle, D. B. & Woodward, C. F. Microstructure and room temperature properties of a high-entropy TaNbHfZrTi alloy. *J. Alloy Compd.* **509**, 6043–6048 (2011).

75. Zhao, Y. Y., Lei, Z. F., Lu, Z. P., Huang, J. C. & Nieh, T. G. A simplified model connecting lattice distortion with friction stress of Nb-based equiatomic high-entropy alloys. *Mater. Res. Lett.* **7**, 340–346 (2019).

76. HajyAkbary, F., Sietsma, J., Böttger, A. J. & Santofimia, M. J. An improved X-ray diffraction analysis method to characterize dislocation density in lath martensitic structures. *Mater. Sci. Eng. A* **639**, 208–218 (2015).

77. Bachmann, F., Hielscher, R. & Schaeben, H. Texture analysis with MTEX – free and open source software toolbox. *SSP* **160**, 63–68 (2010).

78. Vitos, L., Abrikosov, I. A. & Johansson, B. Anisotropic lattice distortions in random alloys from first-principles theory. *Phys. Rev. Lett.* **87**, 156401 (2001).

79. Vitos, L. *Computational quantum mechanics for materials engineers: the EMTO method and applications*. (Springer, 2007).

80. Ranganathan, S. I. & Ostoja-Starzewski, M. Universal elastic anisotropy index. *Phys. Rev. Lett.* **101**, 055504 (2008).

81. Kresse, G. & Furthmüller, J. Efficient iterative schemes for ab initio total-energy calculations using a plane-wave basis set. *Phys. Rev. B* **54**, 11169–11186 (1996).

82. Kresse, G. & Furthmüller, J. Efficiency of ab-initio total energy calculations for metals and semiconductors using a plane-wave basis set. *Comput. Mater. Sci.* **6**, 15–50 (1996).

83. Blöchl, P. E. Projector augmented-wave method. *Phys. Rev. B* **50**, 17953–17979 (1994).

84. Perdew, J. P., Burke, K. & Ernzerhof, M. Generalized gradient approximation made simple. *Phys. Rev. Lett.* **77**, 3865–3868 (1996).

85. Zunger, A., Wei, S.-H., Ferreira, L. G. & Bernard, J. E. Special quasirandom structures. *Phys. Rev. Lett.* **65**, 353–356 (1990).

86. van de Walle, A. et al. Efficient stochastic generation of special quasirandom structures. *Calphad* **42**, 13–18 (2013).

Author contributions

S.M. and Wen C. developed the three-dimensional printing process map and fabricated the as-printed samples. X.F. and P.K.L. fabricated the as-cast samples. S.M. performed mechanical testing of all samples. S.M., X.F., S.S., Y.X., J.S.T., and P.H. performed SEM, EDS, and EBSD characterization and data analyses. S.M., T.L., Y.C., D.Y., and K.A. performed SXRD and neutron-diffraction experiments and analyzed the data. G.K. and Wei C. performed SQS, machine learning, and theoretical calculations of elastic constants. S.M., G.K., X.F., Wei C, and Wen C. drafted the initial manuscript. Wen C. conceived, designed, and led the project. All authors contributed to the data analysis, discussion, and manuscript editing.

Competing interests

The authors declare no competing interests.

Additional information

Supplementary information The online version contains supplementary material available at https://doi.org/10.1038/s43246-024-00452-0.

Correspondence and requests for materials should be addressed to Wei Chen or Wen Chen.

Peer review information *Communications Materials* thanks Sing Swee Leong and the other, anonymous, reviewer(s) for their contribution to the peer review of this work. Primary Handling Editors: Cang Zhao and John Plummer.

Reprints and permissions information is available at http://www.nature.com/reprints